Incommensurate counterrotating magnetic order stabilized by Kitaev interactions in the layered honeycomb α-Li_2IrO_3

S. C. Williams,[1] R. D. Johnson,[1,2] F. Freund,[3] Sungkyun Choi,[1,a] A. Jesche,[3] I. Kimchi,[4] S. Manni,[3,b] A. Bombardi,[5] P. Manuel,[2] P. Gegenwart,[3] and R. Coldea[1]

[1] *Clarendon Laboratory, University of Oxford Physics Department, Parks Road, Oxford, OX1 3PU, United Kingdom*

[2] *ISIS Facility, Rutherford Appleton Laboratory-STFC, Chilton, Didcot, OX11 0QX, United Kingdom*

[3] *EP VI, Center for Electronic Correlations and Magnetism, Augsburg University, D-86159 Augsburg, Germany*

[4] *Department of Physics, Massachusetts Institute of Technology, 77 Massachusetts Ave., Cambridge, Massachusetts 02139*

[5] *Diamond Light Source Ltd., Harwell Science and Innovation Campus, OX11 0DE, United Kingdom*

The layered honeycomb magnet α-Li_2IrO_3 has been theoretically proposed as a candidate to display unconventional magnetic behaviour associated with Kitaev interactions between spin-orbit entangled $j_{\rm eff} = 1/2$ magnetic moments on a honeycomb lattice. Here we report single crystal magnetic resonant x-ray diffraction combined with powder magnetic neutron diffraction to reveal an incommensurate magnetic order in the honeycomb layers with Ir magnetic moments counterrotating on nearest-neighbor sites. This unexpected type of magnetic structure for a honeycomb magnet cannot be explained by a spin Hamiltonian with dominant isotropic (Heisenberg) couplings. The magnetic structure shares many key features with the magnetic order in the structural polytypes β- and γ-Li_2IrO_3, understood theoretically to be stabilized by dominant Kitaev interactions between Ir moments located on the vertices of three-dimensional hyperhoneycomb and stripyhoneycomb lattices, respectively. Based on this analogy and a theoretical soft-spin analysis of magnetic ground states for candidate spin Hamiltonians, we propose that Kitaev interactions also dominate in α-Li_2IrO_3, indicative of universal Kitaev physics across all three members of the harmonic honeycomb family of Li_2IrO_3 polytypes.

PACS numbers: 75.25.-j, 75.10.Jm

I. INTRODUCTION

Magnetic materials in the strong spin-orbit regime are attracting much interest as candidates to display unconventional magnetic states stabilized by frustration effects from bond-dependent anisotropic interactions.[1] One of the most theoretically studied Hamiltonians with bond-dependent interactions is the Kitaev model on the honeycomb lattice, where all bonds carry an Ising exchange, but the three bonds meeting at each lattice site have reciprocally orthogonal Ising axes (along cubic x, y and z directions). This leads to strong frustration effects that stabilize an exactly solvable quantum spin liquid ground state,[2] with unconventional forms of magnetic order predicted to occur when additional magnetic interactions perturb the pure Kitaev limit.[3–6] A_2IrO_3 materials (A=Na, Li) with threefold coordinated, edge-sharing IrO_6 octahedra have been proposed[3,7] as prime candidates to realize such physics as (i) the combination of strong spin-orbit coupling and the near-cubic crystal field stabilize a $j_{\rm eff} = 1/2$ spin-orbit entangled magnetic moment at the Ir site, (ii) for edge-sharing bonding geometry superexchange between neighboring Ir moments is expected to be (to leading order) of Ising form, coupling only the moment components perpendicular to the plane of the Ir-O_2-Ir square plane of the bond, and (iii) the three bonds emerging out of each Ir lattice site have near-orthogonal Ir-O_2-Ir planes. These are key ingredients for frustrated bond-dependent, anisotropic interactions.

The first material to be explored in search of Kitaev physics was Na_2IrO_3, which has a layered crystal structure where edge-sharing IrO_6 octahedra form a honeycomb arrangement. The Ir moments order magnetically[8] at low temperature in a zigzag magnetic structure[9–11] (ferromagnetic zigzag chains ordered antiferromagnetically in the honeycomb plane), which was proposed to be stabilized by many competing interactions.[6] Evidence for Kitaev couplings was provided by the observation of a locking between the spin fluctuations direction and wave vector.[12] Li_2IrO_3 can also be prepared in an isostructural form (α phase, Ref. 13) with Na^+ replaced by Li^+. Furthermore, two other structural polytypes, β- [Ref. 14] and γ-Li_2IrO_3 [Ref. 15] have also been recently synthesized. Both latter structures share the same building blocks of three-fold coordinated, edge-sharing IrO_6 octahedra, but rather than being arranged in honeycomb layers, now the IrO_6 octahedra form three-dimensionally connected structures, called hyperhoneycomb and stripyhoneycomb, respectively. All three polytypes can be systematically understood as members of a "harmonic honeycomb" structural series.[15] This multitude of structural polytypes for Li_2IrO_3 is attributed to the fact that Li^+ and Ir^{4+} have rather comparable ionic radii (Na^+ is a much larger ion, so only the layered honeycomb structure appears to form). Both β- and γ-Li_2IrO_3 show incommensurate magnetic structures with counterrotat-

ing moments,[16,17] understood theoretically to be stabilized by dominant Kitaev interactions and additional small terms;[16,18,19] surprisingly, the β and γ magnetic structures are so similar that they can be considered as "equivalent",[17] leading to proposals of universality of the magnetism in the family of harmonic honeycomb iridates.[20]

Motivated by those ideas we have performed detailed experimental studies of the magnetic order in the layered polytype α-Li_2IrO_3, for which early susceptibility and specific heat measurements in powder samples[21] have indicated magnetic long-range ordering below $\simeq$15 K. No experimental studies of the magnetic structure have been reported so far, however many theoretical proposals have been put forward for rather exotic magnetic structures.[4–6,20,22] On the honeycomb lattice many distinct types of magnetic orders are symmetry allowed, especially for the case of an incommensurate propagation vector, so a complete experimental magnetic structure solution is required in order to provide vital constraints for candidate theoretical models. Using a sample synthesis method not applied to iridates before, we have recently obtained phase-pure, single crystals of α-Li_2IrO_3 and here we report magnetic resonant x-ray diffraction (MRXD) measurements on those crystals, combined with magnetic powder neutron diffraction measurements and symmetry analysis to determine a complete magnetic structure solution. We find an incommensurate magnetic order in the honeycomb layers with counterrotating Ir moments on every nearest neighbor bond. We complement the experimental results with a theoretical soft-spin analysis[20] and propose a minimal nearest-neighbor spin Hamiltonian with dominant Kitaev interactions and additional small terms, which naturally explains the stability of the observed incommensurate structure and the many common features with the magnetic structures in the β and γ polytypes. Our results emphasize that Kitaev interactions between spin-orbit entangled $j_{\rm eff} = 1/2$ Ir^{4+} magnetic moments lead to universal magnetism in all three members of the harmonic honeycomb Li_2IrO_3 polytypes.

The paper is organized as follows. Section II A presents the single-crystal MRXD measurements, which observe magnetic diffraction peaks with an incommensurate propagation vector $\boldsymbol{q} = (0.32(1), 0, 0)$. The observed diffraction pattern is analyzed in terms of magnetic basis vectors, and their polarization and relative phase are determined from the azimuth dependence of the diffraction intensities in Sec. II B. The absolute value of the ordered magnetic moment is extracted from neutron powder diffraction data in Sec. III. The obtained magnetic structure is presented in Sec. IV and similarities with the magnetic structures in the β- and γ-polytypes are discussed in Sec. V. Finally, conclusions are summarized in Sec. VI. The Appendixes contain (A) technical details of the magnetic symmetry analysis and the decomposition of the magnetic structure in terms of its Fourier components, (B) description of the crystal and magnetic

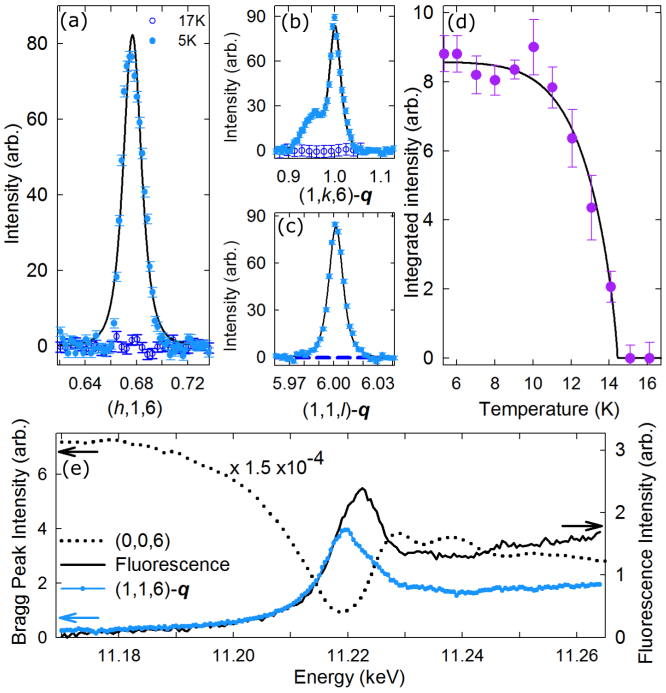

FIG. 1. (color online) Magnetic peak at $(1,1,6)-\boldsymbol{q}$. (a)-(c) Scans along three different reciprocal space directions (filled/open symbols are at base temperature/above $T_{\rm N}$). Solid lines are fits to a Lorentzian-squared shape [panel (b) shows a side shoulder attributed to the finite sample mosaic]. (d) Temperature dependence of the integrated peak intensity (solid line is guide to the eye). (e) Energy scan through the magnetic peak (thick blue solid symbols) showing a large resonant enhancement with a maximum at the onset edge of the fluorescence signal from the sample (black solid line, scaled). In contrast, the same energy scan through a structural peak (dotted line) shows minimum intensity near resonance (due to increased x-ray absorption). Data points in all panels are shown with an estimate of the incoherent background subtracted off.

structure of α-Li_2IrO_3 in terms of the orthorhombic axes common to the β and γ polytypes, (C) derivation of the direct link between the counterrotation of magnetic moments and the antiphase behavior of the MRXD intensity at $\pm\boldsymbol{q}$ magnetic satellites, and (D) a theoretical analysis of the minimal model Hamiltonian that could stabilize the observed magnetic structure in α-Li_2IrO_3.

II. MAGNETIC RESONANT X-RAY DIFFRACTION

A. Experimental results

MRXD experiments were performed using the I16 beamline at Diamond with photon energies near the L_3 edge of Ir. The sample was a single crystal of α-Li_2IrO_3 (maximum dimension $\sim$200 μm, the crystal synthesis and

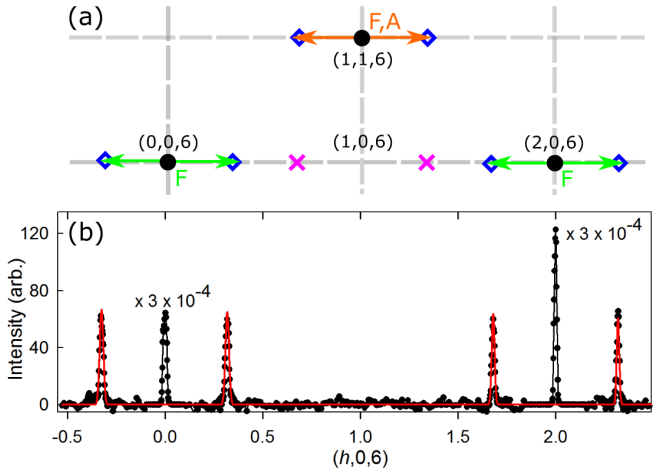

FIG. 2. (a) Schematic diagram of the $(hk6)$ reciprocal plane with filled circles, diamonds and magenta crosses indicating positions of structural peaks, measured magnetic peaks and the absence of peaks, respectively. Lattice points are also labelled by the magnetic basis vectors that have finite structure factor for magnetic peaks at satellite $\pm\boldsymbol{q}$ positions. (b) Scan along the $(h, 0, 6)$ direction observing structural peaks at integer $h = 0, 2$ (intensity scaled by 3×10^{-4} for clarity), and magnetic peaks at satellite positions $h = 0 \pm q, 2 \pm q$. Solid (red) line is the calculated magnetic scattering intensity[25] for the magnetic structure model depicted in Fig. 5. Data points are raw counts with an estimate of the incoherent background subtracted off.

characterization is described elsewhere,[23]) placed with the (001) axis approximately surface normal onto on a Si (111) plate, and cooled using a closed-cycle refrigerator with a Be dome. With the x-ray energy tuned to resonance at 11.217 keV, and the sample temperature set to ≈ 5 K, diffraction peaks were observed at satellite positions $\boldsymbol{\tau} \pm \boldsymbol{q}$ of allowed structural reflections, $\boldsymbol{\tau} = (h, k, l)$ with $h + k =$ even, and with the propagation vector[24] $\boldsymbol{q} = (0.32(1), 0, 0)$. Throughout we label wave vectors in reciprocal lattice units of the structural monoclinic unit cell with space group $C2/m$ (for more details, see Appendix A). A representative scan is shown in Fig. 1(a) (solid circles). Also shown are data points collected at high temperature (17 K, open circles), which illustrate that this diffraction signal is only present at low temperatures. The temperature dependence of the integrated peak intensity is shown in Fig. 1(d), and was found to have a typical order-parameter behavior with an onset temperature $T_{\rm N} = 14.4(2)$ K, which essentially coincides with the transition temperature to magnetic order inferred from earlier specific heat and susceptibility measurements on powder samples.[21] We therefore attribute the satellite peaks to x-ray diffraction from the periodic magnetic order of Ir moments. The satellite peaks were as sharp as structural peaks in scans along all three reciprocal space directions [representative scans shown in Figs. 1(a)-1(c)], indicating coherent, three-dimensional long-range magnetic order. The magnetic origin of the satellite reflections is further confirmed by the intensity dependence on the x-ray energy. Figure 1(e)(blue solid symbols) shows that the peak intensity has a large resonant enhancement, as characteristic of magnetic x-ray diffraction. The empirically observed x-ray resonance energy is similar to values found in other iridates[9,16,17] and agrees well with the edge of the measured fluorescence signal from the sample [black solid line in Fig. 1(e)].

We note that the observed propagation vector $\boldsymbol{q}$ is close to the commensurate wave vector $(1/3, 0, 0)$, which corresponds to an exact tripling of the unit cell along a; however, this commensurate wave vector is not a special high symmetry point in the Brillouin zone of the structural $C2/m$ space group, but has the same symmetry as any general point in the $(h0l)$ plane. In the following analysis of the magnetic structure we therefore treat $\boldsymbol{q}$ as a general incommensurate wave vector. The fact that $\boldsymbol{q}$ has no component along $\boldsymbol{c}^*$ has a natural physical interpretation: adjacent honeycomb layers are stacked ferromagnetically along $\boldsymbol{c}$.

B. Magnetic basis vectors

Systematic surveys in reciprocal space revealed that satellite peaks occurred only around structural Bragg peaks. For example, Fig. 2(b) shows a scan along the $(h, 0, 6)$ direction where the red solid line highlights the observed magnetic peaks at $h = 0 \pm q$ and $2 \pm q$, with no magnetic signal at $h = 1 \pm q$ [magenta crosses in Fig. 2(a); several azimuth values were tested, not shown]. Therefore, the magnetic structure can be fully described in terms of Fourier components of magnetic moments located in the structural primitive cell. α-Li_2IrO_3 has a monoclinic crystal structure with space group $C2/m$ with two Ir atoms in the primitive cell, labeled here as Ir1 at $(0, y, 0)$ and Ir2 at $(0, -y, 0)$ with $y = 0.3332$, where the atomic fractional coordinates are given in the $C2/m$ cell.[13,26] For a propagation vector $\boldsymbol{q} = (q, 0, 0)$ symmetry analysis[27] in the $C2/m$ space group gives two magnetic basis vectors with Fourier components at the two iridium sites in phase or in antiphase, in shorthand notation labeled F and A, respectively. The structure factors for the two basis vectors for a magnetic reflection at wavevector $\boldsymbol{Q} = (h, k, l) \pm \boldsymbol{q}$ are

$$\begin{aligned} \mathcal{S}^F &= 2 f_C \ \cos(2\pi k y), \\ \mathcal{S}^A &= 2 f_C \ i \sin(2\pi k y), \end{aligned} \qquad (1)$$

where the prefactor $f_C = 1 + e^{i\pi(h+k)}$ arises from the C centering in the ab plane. Using the approximation $y \simeq 1/3$ implies that F basis vectors can contribute to magnetic satellites of all structurally allowed peaks $(h + k =$ even$)$, whereas A basis vectors could contribute only to the subset of those with $k \neq 3n$, n integer. Below we use those selection rules and the polarization dependence of the MRXD cross section to determine which basis vectors are present, their polarization, and relative phase.

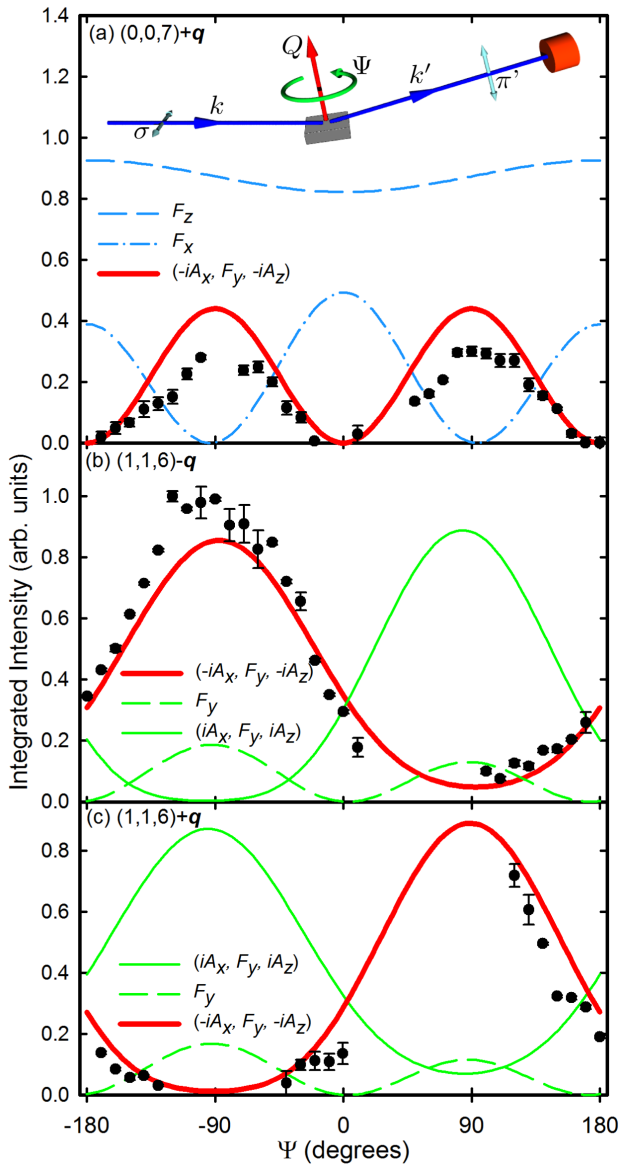

FIG. 3. (color online) Integrated intensity as a function of azimuth for three magnetic Bragg peaks: a) pure-F, b) and c) paired satellites of mixed FA character. Top diagram illustrates the scattering geometry. Data points (filled circles) are integrated peak intensities from rocking curve scans corrected for absorption and Lorentz factor. Thick (red) lines show fits that include all contributions to the MRXD structure factor[25] for the magnetic structure model $(-iA_x, F_y, -iA_z)$, depicted in Fig. 5. Blue/green curves illustrate that other phase combinations of basis vectors are ruled out.

For a σ-polarized incident beam (electric field normal to the scattering plane) only the projection of the magnetic moments onto the scattered beam direction, $\hat{\boldsymbol{k}}'$, contributes to the diffraction intensity.[28] By rotating the sample around the scattering vector, $\boldsymbol{Q} = \boldsymbol{k}' - \boldsymbol{k}$, by the azimuth angle, Ψ, [see diagram in Fig. 3(a), inset] the projection of the magnetic moments onto $\hat{\boldsymbol{k}}'$ changes, giving a clear signature of the moment direction [in the following we employ a convenient Cartesian set of axes (x,y,z) derived from the monoclinic axes, $\boldsymbol{x} \parallel \boldsymbol{a}$, $\boldsymbol{y} \parallel \boldsymbol{b}$ and $\boldsymbol{z} \parallel \boldsymbol{c}^*$, to describe magnetic moment directions]. We have measured the azimuth dependence for three magnetic peaks close to the sample surface normal, such that the Ψ rotation is almost around (001). The origin, $\Psi = 0$, is defined as the azimuth when the (100) direction is in the scattering plane and pointing away from the x-ray source. Figure 3(a) shows the azimuth scan for a pure-F magnetic Bragg peak, $(0,0,7) + \boldsymbol{q}$ ($\mathcal{S}^A|_{k=0} = 0$). The intensity drops to essentially zero at $\Psi = 0$ and $\pm 180°$ and has maxima near $\pm 90°$, uniquely identifying this signal as originating from diffraction by y-moment components, i.e., moments parallel to the crystallographic b axis (solid red line). Scattering from x- and z-moment components (shown by dash-dotted and dashed lines, respectively) have a qualitatively different behavior and can be clearly ruled out. This analysis identifies the presence of a basis vector component F_y and the absence (within experimental accuracy) of F_x and F_z. Figures 3(b) and 3(c) show the azimuth dependence of the intensity for the paired magnetic satellites $(1,1,6) \mp \boldsymbol{q}$, where both F and A basis vectors can contribute. A pure F_y basis vector (dashed line) cannot explain the observed periodicity of the azimuth dependence, and fails to predict the observed antiphase behavior of the intensity of the two satellites. The data is naturally explained by adding an A basis vector component to the magnetic ground state with a comparable magnetic moment magnitude to the F_y component, polarized in the xz plane, and with a $\pi/2$ phase difference. This basis vector combination, namely $(-iA_x, F_y, -iA_z)$, was fit to the data as shown by thick red lines in Figs. 3(a)-3(c), which gives a good account of the observed angular intensity dependence for all three azimuth scans. All other basis vector combinations are ruled out qualitatively by the data as illustrated by various (thin) lines in the figures. The fit gives the relative magnetic moment magnitudes as $M_x : M_y : M_z = 0.12(2) : 1 : 0.74(4)$.

We note that the empirically determined basis vector combination, $(-iA_x, F_y, -iA_z)$, corresponds to a single irreducible representation, Γ_1, as listed in Table I. The form of the magnetic structure is therefore fully consistent with a continuous transition from paramagnetic to magnetic order below T_N.

The absolute magnitude of the ordered magnetic moments is difficult to extract reliably from the MRXD data as it requires accurate determination of scale factors between the magnetic and structural peaks [the latter being $\sim 10^4$ more intense; see Fig. 2(a)]. For this purpose we use neutron diffraction where the structural and magnetic neutron scattering factors are comparable, allowing one to reliably extract the magnetic scattering intensity in absolute units.

TABLE I. Irreducible representations and basis vectors for a magnetic structure with propagation vector $\boldsymbol{q}=(q,0,0)$. The labels in brackets correspond to the Miller and Love notation convention.[29]

Irreducible representation	Basis vectors
$\Gamma_1(\mathrm{B}_1)$	A_x, F_y, A_z
$\Gamma_2(\mathrm{B}_2)$	F_x, A_y, F_z

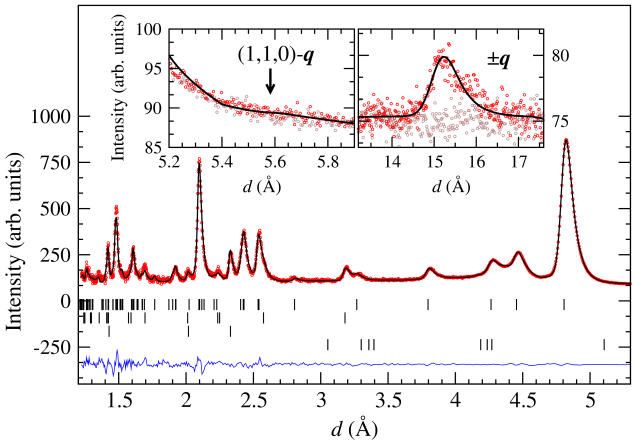

FIG. 4. (color online) Neutron powder diffraction at base temperature (5.9 K, red circles) and in the paramagnetic regime (30 K, brown circles) in the lowest-angle detector bank. The four rows of marks below the pattern show (from top to bottom) positions of structural α-Li_2IrO_3 peaks, impurity phase IrO_2 peaks, aluminium peaks (from the sample sachet), and magnetic Bragg peaks, respectively, and the blue line underneath represents the difference between data and fit. Insets: zoom into the large d-spacing region showing the fundamental magnetic peak indexed as $(000)\pm\boldsymbol{q}$ (right panel). In all panels the solid black line shows the fit (using FullProf[30]) to the structural and magnetic contributions as discussed in the text.

III. NEUTRON POWDER DIFFRACTION

Neutron diffraction measurements were performed on a 1.2 g powder sample of α-Li_2IrO_3 (synthesized as described in Ref. 21) using the time-of-flight diffractometer WISH at ISIS. Powder α-Li_2IrO_3 is susceptible to absorb moisture when in contact with air, which leads to a strong background signal due to incoherent neutron scattering from the absorbed hydrogen. To minimize this effect the sample was heated to a temperature of 110°C under a continuously pumped vacuum (10^{-5} bars) for over 48 h immediately prior to the neutron diffraction experiments. The sample was placed in an aluminium sachet shaped into an annular cylinder (to minimize neutron absorption) and located inside a thin-walled vanadium can. Cooling was provided by a closed cycle refrigerator and the neutron diffraction pattern was collected at a selection of temperatures from base (5.9 K) to paramagnetic (30 K).

Figure 4 shows the measured diffraction pattern in the lowest angle bank of detectors and the right inset shows a zoom of the large d-spacing region where the fundamental magnetic peak indexed as $(000)\pm\boldsymbol{q}$ was clearly observed. We fit simultaneously four contributions to the diffraction data: structural peaks of the sample, structural peaks of an impurity phase identified as IrO_2 (nonmagnetic), structural peaks of the aluminium sachet containing the sample, and magnetic peaks of the sample. The diffraction pattern did not allow for a full refinement of the α-Li_2IrO_3 crystal structure due to relative peak intensities being affected by neutron absorption from iridium nuclei. We therefore fixed the internal atomic positions to those reported by room-temperature x-ray studies,[13] and only refined the lattice parameters and the atomic displacement parameters. This strategy was found to be sufficient for scaling the magnetic moment magnitude. The magnetic structure model deduced from the resonant x-ray data in Sec. II B with the basis vector combination $(-iA_x, F_y, -iA_z)$, and fixed magnitude ratios M_x/M_y and M_z/M_y, was fitted to the data with only the magnetic moment amplitude M_y free to vary. The overall fit is plotted as a solid black line in Fig. 4 and shows excellent agreement with the data, both for the structural pattern (main panel), as well as for the magnetic pattern (insets). In particular, we note that the model accounts very well for the observed strong intensity of the fundamental magnetic peak (right inset) and essentially zero measurable intensity at the nominal position of the second allowed magnetic peak (left inset). The obtained ordered magnetic moment magnitude is $0.40(5)\mu_\mathrm{B}$ when aligned along the b axis, which is a lower bound owing to attenuation of the diffraction peak intensity by Ir absorption. The propagation vector was also fitted and found to be $\boldsymbol{q}=(0.319(5),0,0)$, consistent with the value deduced from single-crystal x-ray measurements.

IV. MAGNETIC STRUCTURE

Having determined the magnetic basis vectors, their amplitudes, and relative phases, the magnetic structure in real space is obtained via Fourier transformation as detailed in Appendix A, Eq. (A2). The resulting magnetic structure for one honeycomb layer is plotted in Fig. 5a). We show the projection along the monoclinic c-axis to better visualize the elliptical envelopes described by the rotation of the magnetic moments when displaced along the (horizontal) propagation direction. The elliptical envelopes have aspect ratio near 3:4 with the long axis along b, and they are oriented in a plane that is almost normal to the ab honeycomb layer (the precise orientation with respect to the honeycomb layer is obtained by rotation around the b axis by an angle $\tan^{-1}\frac{M_z}{M_x} = 80.8\pm1.5°$).

This tilt is illustrated in Fig. 5(b), which shows the projection of the magnetic structure onto the ac plane. An important feature of the magnetic structure highlighted in Fig. 5(a) is that nearest-neighbor sites in the honeycomb lattice counterrotate; this is true both for nearest neighbors of the zigzag chains along a, as well as for vertically connected sites along b; see left curly arrows in the figure. The counterrotation is a direct consequence of the basis vector combination F_y with $iA_{x,z}$, which means that for Ir1 and Ir2 sites in the same primitive cell the y moment components are parallel, whereas their perpendicular components in the xz plane are antiparallel, leading to counterrotation of the moments on the two Ir sublattices. In Appendix C we show that the counterrotation of moments has a characteristic signature in the MRXD intensity via an interference scattering term that alternates in sign between $\pm\boldsymbol{q}$ satellites of the same reciprocal lattice point, which leads to an antiphase behavior of the intensity in azimuth scans. For a given azimuth value, at one satellite the interference term is added and at the other satellite it is subtracted, so when one magnetic satellite is strong the other is weak, and vice versa. This effect is directly observed in our experiments at the paired satellites $(116)\mp\boldsymbol{q}$ in Figs. 3(b) and 3(c), which reveal a pronounced antiphase behavior of the intensity at the two positions; this qualitative behavior of the intensity cannot be explained by any other type of magnetic structure (for more details, see Appendix C).

For a direct comparison between the observed magnetic structure and theoretical models for a two-dimensional honeycomb lattice we show in Fig. 6b) a diagram of the reciprocal space of such a two-dimensional honeycomb, where the blue stars indicate the location of the empirically determined magnetic Bragg peaks of a single honeycomb layer of α-Li_2IrO_3. In this case the magnetic propagation vector has components $(q, 0)$ with reference to a rectangular $a\times b$ unit cell [dashed rectangle in Fig. 6(a)] of the honeycomb lattice.

V. DISCUSSION

Here we discuss the key features of the magnetic structure and possible spin Hamiltonians that could explain its stability. Incommensurate magnetic orders on the honeycomb lattice have been discussed theoretically for various frustrated spin Hamiltonians,[4–6,22,31] however, the observed counterrotation of magnetic moments on every nearest-neighbor bond is a highly nontrivial feature to reproduce theoretically. As explained in Refs. 16 and 20 for a pair of spins that counterrotate the conventional Heisenberg exchange energy is exactly zero at the mean-field level, i.e., if magnetic moments $\boldsymbol{S}_i$ and $\boldsymbol{S}_j$ in the unit cell are counterrotating in a common plane then $\langle J_{ij}\boldsymbol{S}_i\cdot\boldsymbol{S}_j\rangle = 0$, where $\langle\ldots\rangle$ means the average over that type of bond for all unit cells in the crystal. So a spin Hamiltonian based on dominant Heisenberg exchanges cannot explain the observed structure.

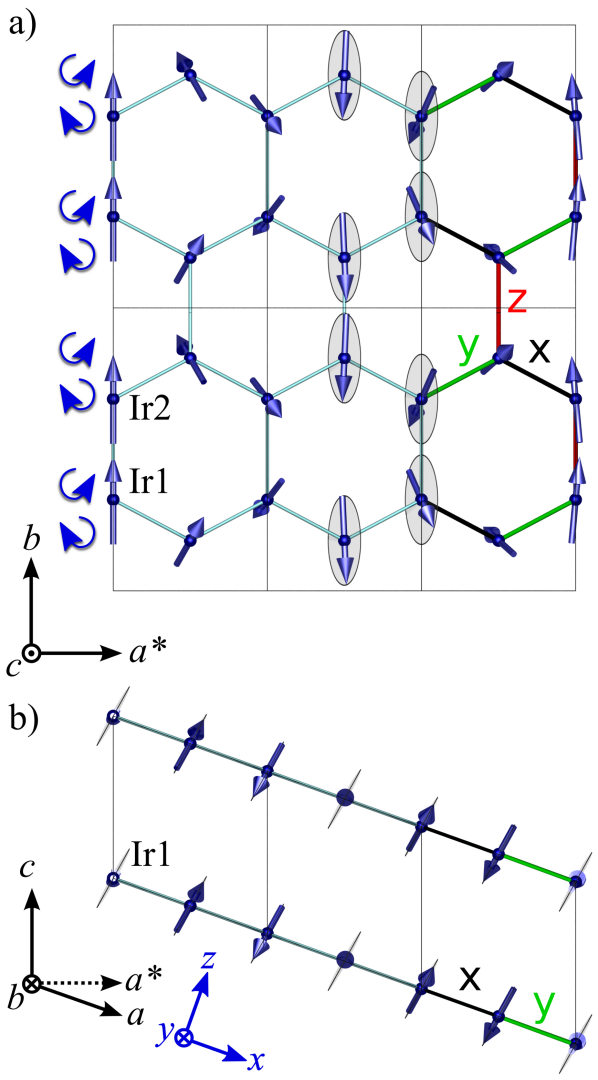

FIG. 5. a) Magnetic structure in a honeycomb layer of α-Li_2IrO_3 viewed along the monoclinic $\boldsymbol{c}$ axis. Three unit cells are shown horizontally (along the propagation direction) and two vertically, with unit cell edges indicated by thin gray rectangles. The global phase of the moment rotation was chosen such as to have the magnetic moments at the origin pointing straight up along the b axis. Left curly arrows illustrate counterrotation of the magnetic moments between consecutive sites along $\boldsymbol{b}$. In unit cell 2 the light shaded ellipses show the envelopes of the moment rotation. In unit cell 3 the color coding of the bonds indicates the anisotropy axes of Kitaev exchange (black, green, red for x, y, z, respectively). (b) Projection of the magnetic structure onto the $\boldsymbol{ac}$ plane showing ferromagnetic order between adjacent layers stacked along $\boldsymbol{c}$. The magnetic propagation vector is along the horizontal direction ($\boldsymbol{a}^*$, dashed arrow). Thin gray lines at each site give the projection of the elliptical envelopes of moment rotation. The Cartesian axes (x, y, z) used to describe the magnetic moment components are shown in blue at the bottom of the figure.

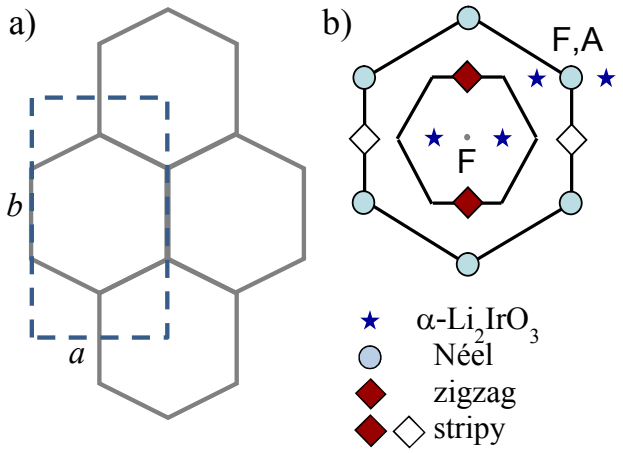

FIG. 6. a) Honeycomb lattice showing the $a \times b$ unit cell (dashed rectangle). b) Reciprocal space diagram of the honeycomb lattice showing the position of the magnetic Bragg peaks (blue stars) corresponding to the incommensurate magnetic order in α-Li_2IrO_3. Labels F and A next to zone center positions $\boldsymbol{\tau}$ indicate the character of the magnetic basis vectors that can contribute to the intensity of the corresponding magnetic Bragg peaks at $\boldsymbol{\tau} \pm \boldsymbol{q}$. The inner solid line hexagon is the first Brillouin zone of the honeycomb lattice, and the other symbols are magnetic Bragg peak positions for other types of magnetic structures such as Néel, "zigzag" with spins ferromagnetically aligned on the zigzag bonds and antialigned along the vertical bonds, and "stripy" with spins ferromagnetically aligned along the vertical bonds and antialigned along the zigzag bonds.

In particular, a Heisenberg model with couplings up to third nearest neighbor can accommodate incommensurate moment-rotating ground states in the phase diagram with propagation vectors along the a axis (the so-called $H1$ and $H3$ phases) or the b axis ($H2$ phase);[31] however, all those phases share the key feature that magnetic moments are corotating, in stark contrast to the experimentally observed magnetic structure. Similarly, The so-called IC_x phase proposed for a model based on frustrated triplet ferromagnetic dimers[22] of α-Li_2IrO_3 does have Bragg peaks with the same selection rules as plotted in Fig. 6(b) (blue stars), however, the ordered moments are corotating, so can also be ruled out. The positions of the magnetic Bragg peaks can rule out other magnetic structure models, such as a "vertex phase"[6] with Bragg peaks at the corners of the first Brillouin zone [inner hexagon in Fig. 6(b)], or an incommensurate magnetic phase[6] continuously connected to the zigzag phase observed in Na_2IrO_3; such an incommensurate structure would have the propagation vector oriented perpendicular to the zigzag chains [of type $(0, k)$, $k < 1$] in the diagram in Fig. 6(b), contrary to the observed wave vector $(q, 0)$, oriented parallel to the zigzag chains.

In order to discuss other spin Hamiltonians that could explain the stability of the observed magnetic structure

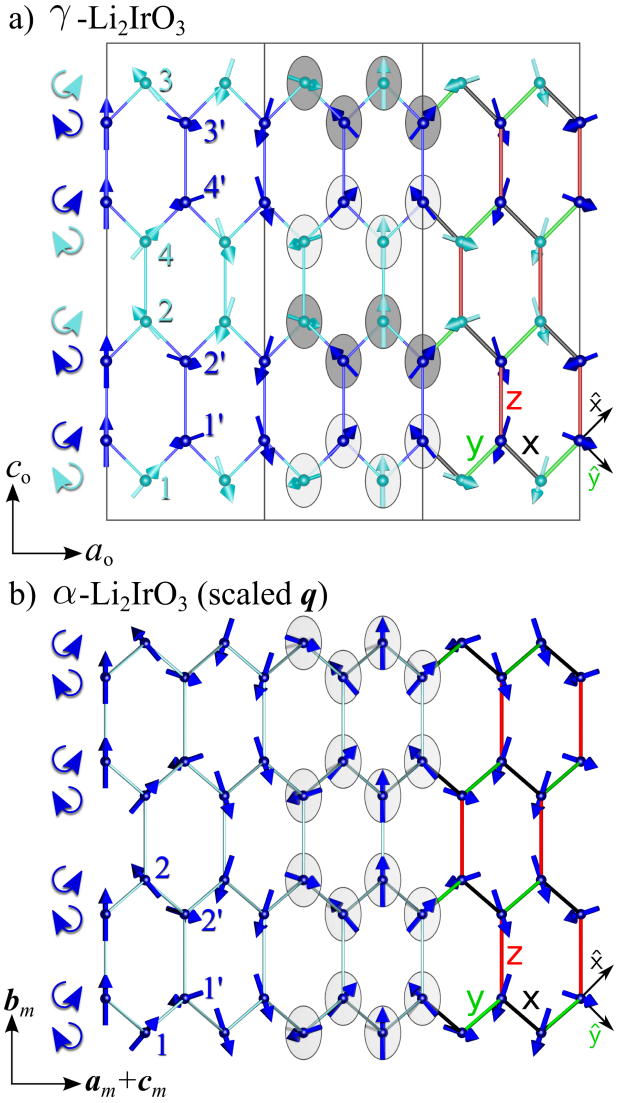

FIG. 7. (a) Magnetic structure in γ-Li_2IrO_3 projected onto the orthorhombic $\boldsymbol{a}_o\boldsymbol{c}_o$ plane (from Ref. 16). (b) For comparison, the magnetic structure in *one* honeycomb layer of α-Li_2IrO_3 is plotted for a scaled propagation vector, $f\boldsymbol{q}$, with $f = 0.89$, such that it shows the same periodicity of moment rotation as in γ-Li_2IrO_3. For both structures left curly arrows indicate counterrotation of moments between consecutive sites along $\boldsymbol{c}_o$ and both magnetic structures are plotted for three orthorhombic cells along the horizontal direction. In (a) light/dark shaded elliptical envelopes in unit cell 2 illustrate the alternation of the orientation of the plane of rotation between adjacent vertically stacked zigzag chains, whereas no such alternation occurs in the α magnetic structure [panel (b)]. In unit cell 3 the color of bonds indicates the anisotropy axis of Kitaev exchange with black/green/red for $\mathsf{x}, \mathsf{y}, \mathsf{z}$. The Kitaev axes are normal to the Ir-O_2-Ir bond planes and are shown by the unit vectors $\hat{\mathbf{x}}$, $\hat{\mathbf{y}}$ ($\hat{\mathbf{z}}$ into the page), as defined in Eq. (B2). In (b) the axes labels $\boldsymbol{a}_m$, $\boldsymbol{b}_m$ and $\boldsymbol{c}_m$ indicate the "symmetrized" monoclinic axes defined in Eq. (B1).

in α-Li_2IrO_3 it is insightful to make a comparison with the magnetic order observed in the β and γ polytypes of Li_2IrO_3, as in all three cases the magnetic order is incommensurate with magnetic moments counterrotating between nearest-neighbor sites. As explained in Ref. 20 the crystal structures of all three polytypes can be described with reference to a common orthorhombic cell, which coincides with the structural cell for the β and γ structures. In this description the Ir honeycomb of the α structure is contained in the diagonal orthorhombic plane $(\boldsymbol{a}_o + \boldsymbol{b}_o, \boldsymbol{c}_o)$, where the subscript o indicates orthorhombic axes. In Fig. 7a-b) we compare the magnetic structures of the γ and α polytypes by looking at their projection onto the orthorhombic $\boldsymbol{a}_o\boldsymbol{c}_o$ plane; this is a convenient comparison as the two iridium lattices are identical in this projection (see Appendix B for details). For α-Li_2IrO_3 [panel (b)] a hypothetical magnetic structure is plotted with the same magnetic eigenvector as found experimentally and plotted in Fig. 5, but for a scaled propagation vector $f\boldsymbol{q}$, where $f \simeq 0.89$, chosen such as to have the same periodicity of the magnetic order as in the γ structure [panel (a)] (for the scaled propagation vector $f\boldsymbol{q}$ the magnetic moment orientation repeats almost every seven zigzag bonds as opposed to a repeat almost every six bonds for the actual α magnetic structure). Direct comparison between the two panels of Fig. 7 shows that, apart from small variations in the moment amplitudes, the two magnetic structures are essentially the same up to a single qualitative difference, which is the fact that the plane of moment rotation is alternating between vertically stacked zigzag chains in the γ phase (see light/dark shading of the elliptical envelopes in unit cell 2), whereas it is not alternating (it is the same for all zigzag chains) in the α phase. In other words, the moment components along the Kitaev z axis (orthorhombic b_o axis) are ferromagnetically aligned for every vertical bond in the γ (and β) structures, whereas they are antiferromagnetically aligned for every vertical bond in the α structure. These two scenarios are clearly differentiated by our experiment. An alternation of the rotation plane would give rise to strong diffraction intensities at satellite positions of structurally forbidden reflections, such as $(106)\pm\boldsymbol{q}$, which were not observed (see Fig. 2).

It has been theoretically proposed that the β and γ magnetic structures are stabilized by a dominant Kitaev exchange supplemented by additional smaller exchange terms,[16,18–20] with the Kitaev term being crucial in stabilizing the counterrotation of moments. The strong similarity of this magnetic structure with the one observed in the α phase suggests that Kitaev interactions are also responsible for the counterrotation of moments in the latter case. In the β and γ structures it is understood that the reason for a tilt of the rotation plane away from the $\boldsymbol{a}_o\boldsymbol{c}_o$ plane is the presence of a finite Kitaev interaction along the vertical (z) bonds $K_\mathsf{z} < 0$ (ferromagnetic), which favors an alternating tilt of the plane of rotation between adjacent zigzag chains.[20] The α magnetic structure also has the plane of rotation tilted away from the $\boldsymbol{a}_o\boldsymbol{c}_o$ plane, but there is no alternation between adjacent zigzag chains.

In Appendix D we perform a soft-spin analysis[20] of the magnetic ground state of candidate spin Hamiltonians that could be compatible with the observed magnetic structure in α-Li_2IrO_3. We start with a minimal nearest-neighbor model that can explain the stability of the magnetic structures in both β and γ phases, with dominant Kitaev interactions K_z along the vertical bonds and $K_{\mathsf{x},\mathsf{y}}$ along the zigzag bonds (all ferromagnetic), an additional smaller (antiferromagnetic) Heisenberg exchange J on all nearest-neighbor bonds, and an Ising (ferromagnetic) coupling I_c on the vertical bonds for the spin components along the bond direction. We find two distinct modifications of the above Hamiltonian that could explain the observed eigenvector and pattern of the magnetic structure in α-Li_2IrO_3. The first modification, model A, has the Kitaev interaction along the vertical bonds having an opposite sign ($K_\mathsf{z} > 0$, antiferromagnetic). The second modification, model B, has uniform Kitaev interactions, but is supplemented by an additional (ferromagnetic) interaction I_d on the zigzag bonds, with $|I_d| < |I_c|$. In both cases, dominant magnitude Kitaev terms are required to stabilize the counterrotation of moments.

VI. CONCLUSIONS

To summarize, combining single-crystal magnetic resonant x-ray diffraction and magnetic powder neutron diffraction on the layered honeycomb α-Li_2IrO_3 we have observed an incommensurate magnetic structure with counterrotating moments for every nearest-neighbor pair of sites. We have discussed that the counterrotation of moments cannot be explained by a spin Hamiltonian with dominant Heisenberg exchange interactions, and we have compared the observed magnetic structure with the incommensurate magnetic orders in the three-dimensional structural polytypes β- and γ-Li_2IrO_3. These two polytypes also have counterrotating moments, proposed theoretically to be stabilized by dominant Kitaev interactions between spin-orbit entangled $j_{\text{eff}} = 1/2$ Ir^{4+} magnetic moments. Based on many striking common features between the magnetic structures in the three polytypes we have suggested that Kitaev interactions are the dominant spin couplings that govern the cooperative magnetism in all three structural polytypes of Li_2IrO_3, and using a soft-spin analysis we have proposed a possible generalization of the spin Hamiltonian used to describe the β and γ structures that could account for the observed magnetic structure in α-Li_2IrO_3.

VII. ACKNOWEDGEMENTS

Work at Oxford was partially supported by the EPSRC (U.K.) under Grants No. EP/H014934/1 and EP/M020517/1. RDJ acknowledges support from a Royal Society University Research Fellowship. IK acknowledges support from an MIT Pappalardo Fellowship. Work at Augsburg was supported by the Helmholtz Virtual Institute 521 ("New states of matter and their excitations") and the German Science Foundation through TRR-80. We thank Diamond Light Source for access to beamline I16 (under Proposal MT12028-1) that contributed to the results presented here. In accordance with the EPSRC policy framework on research data, access to the data will be made available from Ref. 33.

[a] Present address: Max Planck Institute for Solid State Research, Heisenbergstraße 1, 70569 Stuttgart, Germany
[b] Present address: Ames Laboratory, Department of Physics and Astronomy, Iowa State University, Ames, Iowa-50010

[1] J. G. Rau, E. K.-H. Lee, and H.-Y. Kee, Annu. Rev. Condens. Matter Phys. **7**, 195 (2015).
[2] A. Kitaev, Ann. Phys. (N.Y.) **321**, 2 (2006).
[3] J. Chaloupka, G. Jackeli and G. Khaliullin, Phys. Rev. Lett.**105**, 027204 (2010).
[4] J. G. Rau, E. K.-H. Lee, H. Y. Kee, Phys. Rev. Lett.**112**, 077204 (2014).
[5] J. Reuther, R. Thomale, and S. Rachel, Phys. Rev. B**90**, 100405 (2014).
[6] J. Chaloupka and G. Khaliullin, Phys. Rev. B**92**, 024413 (2015).
[7] G. Jackeli and G. Khaliullin, Phys. Rev. Lett.**102**, 017205 (2009).
[8] Y. Singh, P. Gegenwart, Phys. Rev. B**82**, 064412 (2010).
[9] X. Liu, T. Berlijn, W.-G. Yin, W. Ku, A. M. Tsvelik, Young-June Kim, H. Gretarsson, Yogesh Singh, P. Gegenwart, and J. P. Hill, Phys. Rev. B**83**, 220403(R) (2011).
[10] S. K. Choi, R. Coldea, A. N. Kolmogorov, T. Lancaster, I. I. Mazin, S. J. Blundell, P. G. Radaelli, Yogesh Singh, P. Gegenwart, K. R. Choi, S.-W. Cheong, P. J. Baker, C. Stock, and J. Taylor, Phys. Rev. Lett.**108**, 127204 (2012).
[11] F. Ye, S. Chi, H. Cao, B. C. Chakoumakos, J. A. Fernandez-Baca, R. Custelcean, T. F. Qi, O. B. Korneta, and G. Cao, Phys. Rev. B**85**, 180403(R) (2012).
[12] S. H. Chun, J.-W. Kim, J. Kim, H. Zheng, C. C. Stoumpos, C. D. Malliakas, J. F. Mitchell, K. Mehlawat, Y. Singh, Y. Choi, T. Gog, A. Al-Zein, M. Sala, M. Moretti, Krisch, J. Chaloupka, G. Jackeli, G. Khaliullin, and B. J. Kim, Nat. Phys. **11**, 462 (2015).
[13] M. J. O'Malley, H. Verweij and P.M. Woodward, J. Solid State Chem. **181**, 1803 (2008).
[14] T. Takayama, A. Kato, R. Dinnebier, J. Nuss, H. Kono, L.S.I. Veiga, G. Fabbris, D. Haskel, and H. Takagi, Phys. Rev. Lett.**114**, 077202 (2015).
[15] K. A. Modic, T. E. Smidt, I. Kimchi, N. P. Breznay, A. Biffin, S. Choi, R. D. Johnson, R. Coldea, P. Watkins-Curry, G. T. McCandless, J. Y. Chan, F. Gandara, Z. Islam, A. Vishwanath, A. Shekhter, R. D. McDonald, and J. G. Analytis, Nature Comm. **5**, 4203 (2014).
[16] A. Biffin, R. D. Johnson, I. Kimchi, R. Morris, A. Bombardi, J. G. Analytis, A. Vishwanath, and R. Coldea, Phys. Rev. Lett.**113**, 197201 (2014).
[17] A. Biffin, R. D. Johnson, Sungkyun Choi, F. Freund, S. Manni, A. Bombardi, P. Manuel, P. Gegenwart, and R. Coldea, Phys. Rev. B**90**, 205116 (2014).
[18] E. K.-H. Lee and Y. B. Kim, Phys. Rev. B**91**, 064407 (2015).
[19] E. K.-H. Lee, J. G. Rau, Y. B. Kim, arXiv:1506.06746.
[20] I. Kimchi, R. Coldea, and A. Vishwanath, Phys. Rev. B**91**, 245134 (2015).
[21] Y. Singh, S. Manni, J. Reuther, T. Berlijn, R. Thomale, W. Ku, S. Trebst, and P. Gegenwart, Phys. Rev. Lett.**108**, 127203 (2012).
[22] S. Nishimoto, V. M. Katukuri, V. Yushankhai, H. Stoll, U. K. Roessler, L. Hozoi, I. Rousochatzakis, and J. van den Brink, Nat. Commun. **7**, 10273 (2016).
[23] F. Freund, S. C. Williams, R. Coldea, P. Gegenwart, A. Jesche, arXiv:1604.04551.
[24] The uncertainty in the value of q is estimated from combining uncertainties in the crystal orientation (UB-matrix) and the I16 instrument intrinsic sphere of uncertainty.
[25] http://forge.ill.eu/svn/magnetix
[26] We use the nominal crystal structure with no site mixing, where Ir ions occupy the single crystallographic site $4g(0, y, 0)$ in the $C2/m$ cell of Ref. 13.
[27] *BasiReps* software part of the *FullProf* suite[30].
[28] J. P. Hill and D. F. McMorrow, Acta Cryst. A **52**, 236, (1996).
[29] S. C. Miller and W. F. Love, *Tables of irreducible representations of space groups andco-representations of magnetic space groups* (Pruett Press, Boulder, 1967).
[30] J. Rodriguez-Carvajal, Physica B **192**, 55 (1993).
[31] E. Rastelli, Statistical Mechanics of Magnetic Excitations: From Spin Waves to Stripes to Checkerboards (World Scientific, London, 2013), ch. 7.9.
[32] ISOTROPY Software Suite, http://iso.byu.edu
[33] http://dx.doi.org/10.5287/bodleian:0owNjYQnm

Appendix A: Magnetic Symmetry Analysis

Here we give further details of the magnetic symmetry analysis and the description of the magnetic structure using basis vectors, following closely the analysis for β-Li_2IrO_3 in Ref. 17. α-Li_2IrO_3 has a monoclinic crystal structure with space group[13] $C2/m$ and room-temperature lattice parameters $a = 5.1633(2)$ Å, $b = 8.9294(3)$ Å, $c = 5.1219(2)$ Å and $\beta = 109.759(3)°$. The iridium ions occupy a single crystallographic site[26] with multiplicity 4, Wyckoff letter g, and site symmetry 2. There are two iridium atoms per primitive cell, which in the monoclinic C-centered cell correspond to Ir1 at fractional coordinates $(0, y, 0)$, and Ir2 at $(0, -y, 0)$, with $y = 0.3332$. For the magnetic propagation vector $\boldsymbol{q} = (q, 0, 0)$ symmetry analysis using BasiReps[27] gives two types of magnetic basis vectors, F and A, which cor-

respond to the case where the Fourier components, $\boldsymbol{M}_{\boldsymbol{q},n}$, of the magnetic moments of the two iridium sublattices ($n = 1, 2$ for Ir1,2 respectively) are in phase or in antiphase, i.e., $\boldsymbol{M}_{\boldsymbol{q},2} = \pm\boldsymbol{M}_{\boldsymbol{q},1}$ with the upper/lower sign for F/A. The irreducible representations of the magnetic structure and basis vectors are listed in Table I, where (x, y, z) form a Cartesian set of axes related to the monoclinic axes as $\boldsymbol{x} \parallel \boldsymbol{a}$, $\boldsymbol{y} \parallel \boldsymbol{b}$, and $\boldsymbol{z} \parallel \boldsymbol{c}^*$. The magnetic moment distribution in real space is obtained by Fourier transformation, i.e., the magnetic moment on sublattice n at a general position $\boldsymbol{r}$ in the crystal is expressed in terms of the Fourier components as $\boldsymbol{M}_{\boldsymbol{r},n} = \sum_{\boldsymbol{k}=\pm\boldsymbol{q}} \boldsymbol{M}_{\boldsymbol{k},n} e^{-i\boldsymbol{k}\cdot\boldsymbol{r}}$, where $\boldsymbol{M}_{-\boldsymbol{q},n} = \boldsymbol{M}^*_{\boldsymbol{q},n}$ as the magnetic moment distribution is real.

The requirement that the magnetic structure is invariant under symmetry operations of the full group that maps $\boldsymbol{q}$ into $-\boldsymbol{q}$ (in the present case a twofold axis 2_y at the iridium sites) imposes additional constraints onto the relative phases between basis vector components. For an incommensurate propagation vector perpendicular to the twofold axis the symmetry-allowed magnetic structures can be of the following two types: (i) collinear, amplitude-modulated (spin-density-wave type) with magnetic moment either along the y axis or in a general direction in the perpendicular xz plane, or (ii) moment-rotating, with an elliptical envelope with a principal axis along y (no other magnetic structures remain invariant under the 2_y rotation). In particular, for basis vectors belonging to the Γ_1 irreducible representation the allowed phase combinations (verified using the ISODISTORT[32] software) are $(\pm iA_x, F_y, \pm iA_z)$ with unconstrained magnetic moment magnitudes M_x, M_y, and M_z. The experimentally determined magnetic structure $(-iA_x, F_y, -iA_z)$ is indeed one of those combinations. In this case the Fourier components of the magnetic structure are

$$\boldsymbol{M}_{\boldsymbol{q},n} = \left[\mp i\left(\hat{\boldsymbol{x}}\frac{M_x}{2} + \hat{\boldsymbol{z}}\frac{M_z}{2}\right) + \hat{\boldsymbol{y}}\frac{M_y}{2}\right] e^{-i\varphi_0}, \quad \text{(A1)}$$

where the upper (lower) sign is to be used for the $n = 1(2)$ sublattice, $\hat{\boldsymbol{x}}$ indicates a unit vector along the x direction and so on, and φ_0 is a global phase of the magnetic order. The magnetic moment at position $\boldsymbol{r}$ belonging to site index n is obtained via direct Fourier transformation from Eq. (A1) as

$$\begin{aligned}\boldsymbol{M}_{\boldsymbol{r},n} = &\mp\left(\hat{\boldsymbol{x}}M_x + \hat{\boldsymbol{z}}M_z\right)\sin\left(\boldsymbol{q}\cdot\boldsymbol{r} + \varphi_0\right)\\ &+\hat{\boldsymbol{y}}M_y\cos\left(\boldsymbol{q}\cdot\boldsymbol{r} + \varphi_0\right).\end{aligned} \quad \text{(A2)}$$

The above equation describes all iridium sites, including those related by C-centering translations, where $\boldsymbol{r}$ is the actual position of the ion and n is the site index at the equivalent position (1,2) in the primitive unit cell. The magnetic structure near the origin ($\boldsymbol{r} = 0$) for $\varphi_0 = 0$ is plotted in Fig. 5(a) and shows magnetic moments rotating between sites displaced along the (horizontal) propagation direction, and describing an elliptical envelope with a principal axis along $\boldsymbol{b}$. We note that a nonzero global phase φ_0 is equivalent to a shift in the origin along the propagation direction and, therefore, in the incommensurate case, it describes the same global magnetic structure. The invariance of the magnetic structure with respect to a 2_y rotation is most easily visualized in the extended plot in Fig. 7(b), which displays many more unit cells sites (scaling of the propagation vector keeps the symmetry properties unchanged): here one can see that the magnetic structure is invariant upon a twofold rotation around a vertical axis located where the magnetic moment is aligned vertically (the eighth moment along the horizontal zigzag chain), so the magnetic structure is indeed compatible with the full symmetry of the space group.

Appendix B: The crystal and magnetic structure of α-Li_2IrO_3 in the orthorhombic basis

As explained in Ref. 20 the crystal structures of all three polytypes of Li_2IrO_3 could be described in terms of a common orthorhombic unit cell, with lattice vectors (subscript o) related to the monoclinic axes vectors by

$$\begin{aligned}\boldsymbol{a}_o &= \boldsymbol{a}_m + \boldsymbol{c}_m,\\ \boldsymbol{b}_o &= \boldsymbol{a}_m - \boldsymbol{c}_m,\\ \boldsymbol{c}_o &= 2\boldsymbol{b}_m,\end{aligned} \quad \text{(B1)}$$

where the subscript m indicates a "symmetrized" monoclinic cell where the lattice parameters satisfy $a_m : c_m = 1 : 1$ (in the actual crystal structure of α-Li_2IrO_3 this ratio is[13] $1.008 : 1$). The orthorhombic description also has the advantage that the anisotropy (Kitaev) axes associated with each bond (direction normal to the Ir-O_2-Ir planes) are easily visualized, in particular,[15]

$$\begin{aligned}\hat{\mathsf{x}} &= (\hat{\boldsymbol{a}}_o + \hat{\boldsymbol{c}}_o)/\sqrt{2},\\ \hat{\mathsf{y}} &= (\hat{\boldsymbol{a}}_o - \hat{\boldsymbol{c}}_o)/\sqrt{2},\\ \hat{\mathsf{z}} &= \hat{\boldsymbol{b}}_o,\end{aligned} \quad \text{(B2)}$$

where we have assumed an "idealized" crystal structure with cubic IrO_6 octahedra and lattice parameters in ratio $a_o : b_o : c_o = 1 : \sqrt{2} : 3$. We use SansSerif symbols for the Kitaev axes (x,y,z) to distinguish them from the italic symbols (x,y,z), which denote the Cartesian axes used to describe the magnetic structure. The Kitaev axes are shown in unit cell 3 in Figs. 7(a) and 7(b) where the color of the bonds indicates the anisotropy axis of the Kitaev exchange.

The iridium lattices in the Li_2IrO_3 polytypes can be thought of as being constructed from zigzag chains that run along one of the two diagonal directions in the orthorhombic basal plane $\boldsymbol{a}_o \pm \boldsymbol{b}_o$, connected by vertical bonds along $\boldsymbol{c}_o$. In the α structure all zigzag chains are in the diagonal plane ($\boldsymbol{a}_o$+$\boldsymbol{b}_o$,$\boldsymbol{c}_o$), and are connected vertically to form a honeycomb lattice. In the γ structure pairs of zigzag chains form coplanar honeycomb strips [$33'$ with $11'$ and $22'$ with $44'$ in Fig. 7(a)] that are then

stacked along the vertical direction $\boldsymbol{c}_o$ alternating in orientation between the two diagonal planes ($\boldsymbol{a}_o$+$\boldsymbol{b}_o$,$\boldsymbol{c}_o$) and ($\boldsymbol{a}_o-\boldsymbol{b}_o$,$\boldsymbol{c}_o$); in the β structure single zigzag chains alternate in orientation between the two diagonal directions. From this description it follows that the projection onto the $\boldsymbol{a}_o\boldsymbol{c}_o$ and $\boldsymbol{b}_o\boldsymbol{c}_o$ planes is then the same in all three structures (the projections onto the $\boldsymbol{a}_o\boldsymbol{b}_o$ plane are different).

In the orthorhombic axes notation, the Fourier components of the magnetic structure in Eq. (A1), with the choice for the global phase $\varphi_0 = 0$, are

$$\boldsymbol{M}_{\boldsymbol{q},n} = \mp i\left(\hat{\boldsymbol{x}}_o\frac{M_{x_o}}{2} - \hat{\boldsymbol{y}}_o\frac{M_{y_o}}{2}\right) + \hat{\boldsymbol{z}}_o\frac{M_{z_o}}{2}, \qquad \text{(B3)}$$

where the upper/lower sign is to be used for the sublattices Ir1/Ir2 (which correspond to sites $1'/2'$, respectively, in the γ structure; see Fig. 7) and $M_{x_o} = M_x\cos(\beta/2) + M_z\sin(\beta/2)$, $M_{y_o} = -M_x\sin(\beta/2) + M_z\cos(\beta/2)$, and $M_{z_o} = M_y$. Here $\hat{\boldsymbol{x}}_o$, $\hat{\boldsymbol{y}}_o$, $\hat{\boldsymbol{z}}_o$ are unit vectors along the orthorhombic $\boldsymbol{a}_o$, $\boldsymbol{b}_o$, and $\boldsymbol{c}_o$ axes. For the determined magnetic structure the moment magnitudes are M_{x_o}:M_{y_o}:M_{z_o}=0.67:0.33:1 and the moment rotation plane makes an angle $\phi = \tan^{-1}(M_{y_o}/M_{x_o}) = 26°$ with the $\boldsymbol{a}_o\boldsymbol{c}_o$ plane. The magnetic moment expression, Eq. (A2), transforms to

$$\boldsymbol{M}_{\boldsymbol{r},n} = \mp\left(\hat{\boldsymbol{x}}_o M_{x_o} - \hat{\boldsymbol{y}}_o M_{y_o}\right)\sin\boldsymbol{q}\cdot\boldsymbol{r} + \hat{\boldsymbol{z}}_o M_{z_o}\cos\boldsymbol{q}\cdot\boldsymbol{r}. \qquad \text{(B4)}$$

Appendix C: Counterrotation of moments and the interference term in the scattering cross-section

Here we present an intuitive explanation of the antiphase behavior of the magnetic scattering intensity between the satellites at $(116)\pm\boldsymbol{q}$ illustrated in Figs. 3(b) and 3(c), namely at azimuth values Ψ where the $+\boldsymbol{q}$ satellite is strong the $-\boldsymbol{q}$ satellite is weak, and vice versa. We will show that this qualitative feature of the magnetic scattering can only be explained by counterrotating moments on the two Ir magnetic sublattices. In this case the scattering intensity contains an interference term that changes sign between the two satellite positions, naturally explaining the observed intensity behavior.

To highlight the main terms in the scattering cross-section we first assume $M_x = 0$, i.e., we neglect the contribution from the small moment components along the x direction. In this case the total magnetic structure factor vector for a magnetic satellite at $\boldsymbol{Q} = (h,k,l)\pm\boldsymbol{q}$ is

$$\boldsymbol{\mathcal{F}}(\boldsymbol{Q}) = \hat{\boldsymbol{y}}\mathcal{S}_y M_{y,\pm\boldsymbol{q},1} + \hat{\boldsymbol{z}}\mathcal{S}_z M_{z,\pm\boldsymbol{q},1}, \qquad \text{(C1)}$$

where $\mathcal{S}_{y/z}$ are the structure factors of the magnetic basis vectors along the y/z directions, $M_{y/z,\pm\boldsymbol{q},1}$ are the corresponding Fourier components of the magnetic moments on the Ir1 sublattice and (x,y,z) are Cartesian axes fixed with respect to the crystal axes, as defined previously. Without loss of generality we take $M_{y,\pm\boldsymbol{q},1} = M_y/2$ and $M_{z,\pm\boldsymbol{q},1} = e^{\pm i\varphi}M_z/2$, where $M_{y/z}$ are the (real) magnetic moment magnitudes along the y/z axes and φ is the relative phase between the y and z components, constrained by symmetry to be an integer multiple of $\pi/2$ (see Appendix A).

In the experimental scattering geometry employed, as indicated in Fig. 3 (inset), the magnetic Bragg peak intensity depends only on the projection of the total magnetic structure factor vector $\boldsymbol{\mathcal{F}}$ onto the scattered wavevector direction $\hat{\boldsymbol{k}}'$; see Ref. 28. In detail, the intensity is proportional to

$$\left|\boldsymbol{\mathcal{F}}\cdot\hat{\boldsymbol{k}}'\right|^2 = [\left|\hat{k}'_y M_y\mathcal{S}_y\right|^2 + \left|\hat{k}'_z M_z\mathcal{S}_z\right|^2 + 2\hat{k}'_y\hat{k}'_z M_y M_z\mathcal{A}]/4, \qquad \text{(C2)}$$

where the first two terms are the separate magnetic scattering intensities from the y and z moments, and the last term is due to interference scattering between the y and z moments. The intensity dependence on the azimuth comes exclusively from the projections $\hat{k}'_y$ and $\hat{k}'_z$ of $\hat{\boldsymbol{k}}'$ onto the y and z directions, respectively. The interference term in eq. (C2) is directly sensitive to the basis vector combination through the factor

$$\mathcal{A} = \mathcal{R}\cos\varphi \pm \mathcal{I}\sin\varphi, \qquad \text{(C3)}$$

where $\mathcal{R}$ and $\mathcal{I}$ are the real and imaginary parts of the product $\mathcal{S}_y\mathcal{S}_z^*$ and the upper/lower sign corresponds to the $\pm\boldsymbol{q}$ satellite. If the interference factor $\mathcal{A}$ cancels, then the azimuth dependence of the intensity in Eq. (C2) is essentially the same between paired satellites [up to variations in the geometrical factors between the two satellites, which are expected to be small if the two wavevectors are close, i.e., if $|(hkl)| \gg |\boldsymbol{q}|$]. To obtain a large intensity difference between paired satellites the interference term needs to be large and to alternate in sign between the two satellites, i.e., $\mathcal{I}\sin\varphi \neq 0$ in eq. (C3). Below we analyze all possible combinations of basis vectors and relative phases and find that a sign-alternating interference term occurs only if the basis vectors along the two directions are of different type and are $\pi/2$ out of phase, which corresponds to magnetic structures with counterrotating moments on the two sublattices. This follows from the fact that the magnetic structure factors for the two basis vectors in Eq. (1) are either purely real (F) or purely imaginary (A), so the product $\mathcal{S}_y\mathcal{S}_z^*$ is purely real ($\mathcal{R}\neq 0$ and $\mathcal{I} = 0$) if the basis vectors along the two directions are the same, or purely imaginary ($\mathcal{R} = 0$ and $\mathcal{I}\neq 0$) if they are different. Based on this observation we identify the following four distinct cases summarized in Table II.

(i) Same basis vectors along the two directions with relative phase $\varphi = 0$ or π, the magnetic structure is a spin-density wave (SDW), collinear between the two sublattices, the interference term factor is finite and has the same sign for paired satellites.

(ii) Different type basis vectors with relative phase $\varphi = 0$ or π, each sublattice has a spin-density-wave order, but noncollinear between the two sublattices, there is no interference term.

TABLE II. Properties of the interference factor $\mathcal{A}$ in the magnetic scattering intensity in Eq. (C2) at $(hkl)\pm\boldsymbol{q}$ as a function of the magnetic basis vector combination in the ground state.

Basis Vectors	Phase φ	Magnetic Structure	Interference factor $\mathcal{A}$
FF AA	$0,\pi$	collinear SDW	$\mathcal{R}\cos\varphi$
FA	$0,\pi$	non-collinear SDW	0
FF AA	$\pi/2,-\pi/2$	co-rotating	0
FA	$\pi/2,-\pi/2$	counterrotating	$\pm\mathcal{I}\sin\varphi$

(iii) Same basis vectors on the two directions with relative phase $\varphi=\pi/2$ or $-\pi/2$, magnetic moments co-rotate on the two sublattices (the sign of φ gives the absolute sense of rotation on the Ir1 sublattice), here also there is no interference term.

(iv) Different basis vectors with relative phase $\varphi=\pi/2$ or $-\pi/2$, magnetic moments counterrotate on the two sublattices, the interference term is finite, sign-alternating between paired satellites and with the absolute sign determined by whether the rotation at site Ir1 is clockwise or counterclockwise.

The observation of an antiphase behavior of the intensity between the paired satellites at $(116)\pm\boldsymbol{q}$ [see Figs. 3(b) and 3(c)] can only be explained by a magnetic structure of type (iv) above, with counterrotating moments. The effect can be understood in terms of a sign-alternating interference scattering term between the y and z magnetic moment components, coupled in basis vectors of F and A type, respectively, with a relative phase $\varphi=-\pi/2$ [in the main text we have used the shorthand notation $(F_y,e^{i\varphi}A_z)$ to denote this basis vector combination]. Since the wave vector $\boldsymbol{Q}$ is close to the z axis the azimuth dependence of the geometrical factors are (to leading order) $\hat{k}'_z\simeq\sin\theta$ and $\hat{k}'_y\simeq-\cos\theta\sin\Psi$, where 2θ is the total scattering angle; so the largest magnitude interference term in Eq. (C2) (largest contrast between the intensities of the paired satellites) is expected for Ψ near $\pm90^\circ$, as indeed observed. The red solid lines in Figs. 3(b) and 3(c) show the calculated intensity including the full azimuth dependence of the geometrical factors and also the effect of the small, but finite M_x moment components.

Appendix D: Minimal spin Hamiltonian for α-Li_2IrO_3

Here we study a range of minimal spin Hamiltonians, based on nearest-neighbor exchanges only, seeking to capture the observed incommensurate magnetic structure. The important features can be qualitatively summarized as follows: (1) counterrotation between the Ir1/2 sublattice moments and (2) uniformly tilted plane of rotation. Here by "plane of rotation" we refer to the plane in the Bloch sphere spanned by the various magnetic moments across the lattice; using the orthorhombic axes notation as in Eq. (B4), this is the plane spanned by the vectors $(\hat{\boldsymbol{x}}_o M_{x_o}-\hat{\boldsymbol{y}}_o M_{y_o})$ and $\hat{\boldsymbol{z}}_o$. Feature (1) has been previously shown[20] to require anisotropic (i.e., non-Heisenberg) nearest-neighbor exchange and in particular is consistent with strong Kitaev exchange. In a minimal nearest-neighbor model feature (1) can be captured[20] by (ferromagnetic) Kitaev exchanges on all nearest neighbor bonds K_z, $K_{x,y}<0$, a smaller (antiferromagnetic) Heisenberg exchange $J>0$ on all those bonds, and a finite (ferromagnetic) exchange $I_c<0$ for the vertical bonds, which couples the moment components along the bond direction. Here we discuss modifications that are appropriate for feature (2).

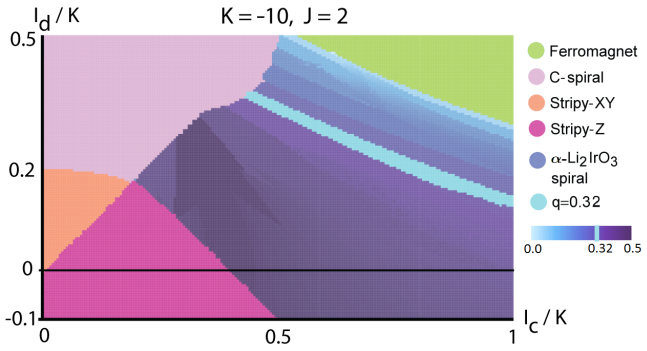

FIG. 8. (color online) Phase diagram of model B described in the text, computed in a soft spin approximation. We find that the observed counterrotating magnetic order ($q=0.32$, light blue line), with a uniformly tilted plane of rotation, can be captured by adding "truncated-dipole" superexchange interactions, I_d and I_c, within the regime $|I_c|>|I_d|$, $I_d/K>0$. These interactions couple spins to the spatial honeycomb plane, which combines with the counterrotation due to Kitaev exchange to produce the experimentally observed magnetic order pattern. The observed spiral phase is shown in a color gradient corresponding to the magnitude of the propagation vector q, from 0 to 0.5 in units of $2\pi/a$. Comparing to Fig. 6(b), the wave vector is along the horizontal direction, with units such that $q=1$ would correspond to the white diamond symbol. Labels stripy-XY and stripy-Z denote antiferromagnetic patterns where spins are aligned with one of their three nearest neighbors, across a diagonal/vertical bond for stripy-XY/Z, respectively, and antialigned with the other two. Label C-spiral denotes an incommensurate counterrotating order with propagation vector along the Γ-M line, e.g., the vertical $(\hat{\boldsymbol{c}}_o=\hat{\boldsymbol{b}}_m)$ direction in Figs. 6(a) and 6(b).

We have found two independent modifications that can produce feature (2) in a dominant-Kitaev Hamiltonian. In general, both modifications could occur and could complement each other. Here we consider them separately. The first modification, denoted as model A, con-

sists of a sign change for the Kitaev exchange on "vertical" bonds, i.e., those bonds which lie parallel to the crystalline $\boldsymbol{c}_o$ (or equivalently $\boldsymbol{b}_m$) axis, i.e., $K_z > 0$. In this model, the $\boldsymbol{b}_o$-axis moment components would be antialigned along those bonds, straightforwardly producing the observed tilt pattern.

The second modification, denoted as model B, consists of an additional weaker exchange on the zigzag bonds, i.e., the nearest-neighbor bonds that are not parallel to the crystalline $\boldsymbol{c}_o$ axis. This exchange, which we denote by I_d, is a symmetry-allowed nearest-neighbor exchange, which couples the spin components pointing along the bond direction

$$I_d S_i^r S_j^r \ , \quad S^r \equiv \boldsymbol{S} \cdot \hat{\boldsymbol{r}} \tag{D1}$$

where $\boldsymbol{r}$ is the vector connecting sites i and j. This exchange interaction has a form that is mathematically analogous to a truncated dipole interaction (though its physical origin is through superexchange). It is related to the Γ spin exchange term that has been previously discussed in the context of the layered honeycomb iridates.[4,20] We use the subscripts on I_c and I_d to denote that the value of the exchange can differ between the "vertical" (along $\boldsymbol{c}_o$) and the remaining (zigzag or "diagonal") bonds.

Here we start with a model with dominant ferromagnetic Kitaev exchanges, which for simplicity we take to have the same magnitude (and sign) on all three nearest-neighbor bonds ($K_{\mathrm{z}} = K_{\mathrm{x,y}} = K < 0$), and an additional small antiferromagnetic Heisenberg exchange J on all those bonds. We find that adding ferromagnetic I_c and I_d exchanges (i.e., of the same sign as the Kitaev exchange) can stabilize the observed counterrotating magnetic order with a uniformly tilted plane of rotation, if $I_d/K > 0$ and $|I_c| > |I_d|$.

A representative soft-spin phase diagram is shown in Fig. 8. The observed α-Li_2IrO_3 counterrotating order is seen across a range of parameters, with a propagation vector that varies continuously across the parameter space, and which includes the experimentally observed value (light blue shading). The lowest energy mode in this phase is seen to have a plane of rotation that is tilted uniformly. The sign of the tilt agrees with the sign observed experimentally, namely it is a small tilt, away from the $\boldsymbol{a}_o\boldsymbol{c}_o$ plane, in the direction away from the plane of the honeycomb lattice.

Within the soft spin approximation, the magnitude of the tilt angle is seen to be about half of the experimentally observed value for typical parameter points with the observed wave vector, and in general varies across the phase as the I_d interactions are turned on. However, we note that the soft spin ground state here requires the spins to be soft and have nonuniform magnitude, representing strong thermal or quantum fluctuations, and thus it is not expected to capture the tilt angle quantitatively. For instance, a sample set of Hamiltonian parameters can be chosen as

$$K = -10,\ J = 2,\ I_c = -5,\ I_d = -3.5 \tag{D2}$$

(where the energy unit may be taken as $\sim$0.45 meV in order to match the observed T_{N}). For those parameters the propagation vector agrees with the experimental value $q = 0.32(1)$ and the ordered spin magnitudes, using the orthorhombic axes as per eq. (B4), are found to be in the ratio

$$S_{x_o} : S_{y_o} : S_{z_o} = 0.56 : 0.15 : 1. \tag{D3}$$

The qualitative feature of uniform tilt is captured by this analysis, and may be understood as resulting from the uniform spatial plane of the honeycomb lattice: the I_c and I_d exchanges couple the spins to the orientation of the bonds on the honeycomb lattice, and can thereby produce this uniform tilt. The sign of the tilt, which is set to be away from the honeycomb plane, is produced by the counterrotation of adjacent sublattices, which sets the $\boldsymbol{b}_o$ components of spins to be anti-aligned between neighboring sites [as per Eq. (B4)], and is thus tilted away from the spatial honeycomb plane by a small ferromagnetic I_d exchange.